The beta propellers of eIF3b and eIF3i relocate together to the ribosomal intersubunit interface during translation initiation

Jose L. Llácer[1,5*†], Tanweer Hussain[2*], Yuliya Gordiyenko[1], Jon R. Lorsch[3], Alan G. Hinnebusch[4] and V. Ramakrishnan[1]

[1]MRC Laboratory of Molecular Biology, Cambridge CB2 0QH, United Kingdom

[2]Molecular Reproduction, Development and Genetics (MRDG), Biological Sciences Building, Indian Institute of Science, Bangalore-560012, India.

[3]Laboratory on the Mechanism and Regulation of Protein Synthesis, Eunice K. Shriver National Institute of Child Health and Human Development, National Institutes of Health, Bethesda, Maryland 20892, USA

[4]Laboratory of Gene Regulation and Development, Eunice K. Shriver National Institute of Child Health and Human Development, National Institutes of Health, Bethesda, Maryland 20892, USA

[5]Instituto de Biomedicina de Valencia (IBV-CSIC), Valencia 46010, Spain

*These authors contributed equally to this work

[†]Correspondence to jllacer@ibv.csic.es

Running title: eIF3b and eIF3i relocate together to the ribosomal intersubunit surface during initiation

Summary

During translational initiation in eukaryotes, the 40S ribosomal subunit forms a 48S pre-initiation complex (PIC) with eIF1, eIF1A, eIF3, ternary complex (eIF2-GTP-Met-tRNA$^{Met}_{i}$) and eIF5. The 48S PIC, in an open conformation, scans the 5' untranslated region of mRNA until it encounters a start codon in the P site. We present a single particle cryo-electron microscopy (cryo-EM) reconstruction of a 48S PICs from yeast in an open scanning-competent state at 5.15 Å resolution. The structure contains eIF3 PCI domains bound on the solvent side of the 40S, that was not observed in the earlier reported complex in an open state. eIF3b is observed bound on the 40S subunit interface, re-located with eIF3i from their solvent-interface locations observed in other PIC structures; however, the eIF3i β-propeller is not in contact with the 40S. We also present a map obtained by masked classification with signal subtraction around the observed β-propeller of eIF3b on the intersubunit interface of our previous 48S PICs in closed state, which also shows similar re-location of eIF3b and eIF3i from the solvent interface. Overall, the structures reported here are similar to those reported earlier but the relatively higher resolution of 48S PIC-open and the higher local resolution around the eIF3 β-propellers in py48S-closed enabled a more detailed assignment of eIF3 subunits and revealed relocation of the entire quaternary complex of eIF3b/eIF3i/eIF3g/eIF3a-Cter to the intersubunit interface of 40S.

Introduction

Eukaryotic translational initiation is a complicated process that involves a complex of the 40S subunit and initiation factors binding to the 5′ end of mRNA and scanning the mRNA until a start codon is encountered in the ribosomal P site (Hinnebusch, 2017). First, eIF1, eIF1A and eIF3 bind to the 40S. The binding of eIF1 and eIF1A facilitate the binding of initiator tRNA ($tRNA_i$) as a ternary complex (TC) with eIF2-GTP. eIF5, a GTPase activating protein (GAP) may be recruited along with TC or in complex with eIF3. The 43S preinitiation complex (PIC) thus formed is recruited to the capped 5′ end of mRNA by the multisubunit eIF4F complex, which consists of the cap-binding protein eIF4E, eIF4G, eIF4B and the helicase eIF4A. This 48S PIC in an open (P_{OUT}) conformation then scans the mRNA until a start codon is encountered. GTP bound in eIF2 can be hydrolysed during the scanning process, however, the phosphate (P_i) product remains bound. Recognition of the start codon leads to a conformational change in the PIC to form a scanning-arrested closed (P_{IN}) complex accompanied by the release of eIF1 and attendant dissociation of P_i (Hinnebusch, 2014; Hinnebusch, 2017; Aylett and Ban, 2017).

Previously, we reported the cryo-EM structure of partial yeast 48S PIC complexes in an open, scanning-competent state (P_{OUT}; hereafter referred to as "py48S-open") at an overall resolution of 6.0 Å (Llácer et al., 2015). It showed density for eIF1, eIF1A, TC including eIF2β, and portions of eIF3. However, the PCI domains of eIF3a and eIF3c on the solvent surface were not observed. Also, portions of eIF3 bound on the subunit-joining interface of the 40S were observed at lower local resolution. Hence, we decided to collect a larger data set with an improved sample (mentioned below) to obtain a map of the 48S PIC in an open conformation at a higher resolution, which will be helpful for a more detailed assignment of eIF3 subunits. Also, certain image processing procedures that were unavailable earlier, including signal subtraction and 3D classification using masks (Bai et al., 2015), enabled us to obtain superior and more homogenous 3D classes. Here we present a structure of yeast 48S PIC in an open scanning-competent state with density for eIF3 PCI domains bound on the solvent side of the 40S and density for quaternary complex of eIF3b/eIF3i/eIF3g/eIF3a-Cter bound on the intersubunit surface of 40S. A similar position of quaternary complex of eIF3b/eIF3i/eIF3g/eIF3a-Cter on the intersubunit interface of 40S was also observed in the map obtained by masked classification with signal subtraction around the observed β-propeller of eIF3b of our previous 48S PICs in closed state

(Llácer et al., 2015). Thus, we show that the whole quaternary complex of eIF3b/eIF3i/eIF3g/eIF3a-Cter re-locates from the solvent surface to the intersubunit interface of 40S.

Results

In order to trap the yeast 48S PIC in an open conformation, we improved the reconstitution of this complex by including an unstructured capped 49-mer mRNA with an AUC start codon (5′GGG[CU]$_3$[UC]$_4$UAACUAUAAAA**AUC** [UC]$_2$UUC[UC]$_4$GAU 3′) in place of the 25-mer uncapped mRNA used earlier. Moreover, eIF4 complex was reconstituted with recombinant, purified eIF4E-eIF4G, eIF4A and eIF4B and the reconstituted eIF4 complex was used to activate the mRNA. The resulting eIF4-mRNA complex was then mixed with pre-formed 43S PIC to form 48S PICs. In assembling 43S PICs, we used eIF3 purified from yeast with a modified purification protocol that minimizes co-purification of eIF5 rather than the recombinant eIF3 expressed in bacteria used in our earlier study, which lacked N-terminal residues for eIF3c and eIF3g (Llácer et al., 2015). Cryo-grids were prepared, a large data set of more than 2600 images were collected, and signal subtraction and 3D classification using masks were used during image processing to obtain a 48S PIC in an open conformation at an overall resolution of 5.15 Å (Figures 1A, 1B and S1). This complex, henceforth termed ‘py48S-open-eIF3’ PIC, is similar to that of the py48S-open PIC described previously (Llácer et al., 2015) except for the presence of clear density for the PCI domains of eIF3 at the solvent side and improved density for eIF3 domains at the subunit-interface. py48S-open-eIF3 and the py48S-open complex reported earlier have similar conformations of the small subunit and positioning of all non-eIF3 factors, except for a few extra residues of the eIF1 N-terminal tail observed approaching and making contacts with eIF2γ in the new map (Figure 1C). Hence, we shall only discuss here the PCI domains of eIF3, not observed earlier, and the eIF3 domains observed at the subunit-interface at higher resolution.

The aforementioned newly available image processing tools were also used to reprocess our earlier reported ‘py48S-closed’ PIC (Figure S1) to obtain a map at an overall resolution of 5.75 Å resolution showing clear densities for the different eIF3 domains at the 40S subunit interface,

henceforth termed 'py48S-closed-eIF3' PIC (Figure 1D). The resolution of 'py48S-closed-eIF3' PIC map is lower than the previous reported 'py48S-closed' PIC map probably because of the relatively smaller number of particles used in this reconstruction (12,732 vs. 21,401 particles). However, the particles seem to be more homogenous for the different eIF3 domains at the subunit interface of the 40S. Hence, we obtained much improved density (Figure S2) for these eIF3 domains despite overall lower resolution for the whole PIC. A closed conformation of the 48S PIC was observed similar to the earlier reported py48S-closed complex (Llácer et al., 2015), and eIF3 is observed in the same conformation as for the new py48S-open-eIF3 PIC (Figure S1). Similarly, we shall only discuss the densities corresponding to eIF3 domains located at the 40S subunit interface in the py48S-closed-eIF3 map since these are the only parts of the map with better local resolutions when compared to those in our previously reported py48S-closed map.

PCI domains of eIF3a and 3c bound on the solvent surface of 40S

The density for the PCI domains of eIF3a and 3c are clearly observed in py48S-open-eIF3 (Figures 1A and 2A). The overall positions of these domains are similar to those observed in the py48S-closed complex (Figures 1A, 1D and 2A, inset). It is likely that using eIF3 purified from yeast for reconstituting the 48S complex and also applying an eIF3 mask for 3D classification during image processing has helped in isolating a class of particles with higher occupancy of eIF3. Though clear density for the PCI domains was observed, no clear density corresponding to the eIF3b β-propeller was observed on the solvent side near helix 16 (h16), in contrast to our earlier reported py48S-open PIC map (Llácer et al., 2015) where a weak density at low resolution was observed near that helix.

eIF3b bound on the subunit interface of 40S

The density for eIF3 domains at the subunit interface is more resolved in py48S-open-eIF3 and py48S-closed-eIF3 maps (Figures 1A, 1D and S2). Density for a β-propeller on the 40S interface near h14 and h44 and in contact with eIF2γ was observed, as reported earlier (Llácer et al., 2015) (Figures 1A, 1C, 1D and 2B). Previously, we had tentatively assigned this density to the β-propeller of eIF3i since partial density for the β-propeller of eIF3b could be seen at its well-

known location at the 40S solvent interface near h16. However, this density near h14 and h44 was re-interpreted as the eIF3b β-propeller by docking an improved mammalian model of eIF3b in the yeast 'py48S-closed' PIC map (Simonetti et al., 2016). These workers were guided by the observation that the β-propeller of eIF3i appeared to be bound instead at the GTPase binding site on the subunit interface in the mammalian 48S late stage IC described in their study (Simonetti et al., 2016). However, this density assigned to the eIF3i β-propeller was later also re-interpreted as ABCE1 protein (Heuer et al., 2017; Mancera-Martínez et al., 2017; Valášek et al., 2017). In view of these previous difficulties in identifying the β-propellers of eIF3i and eIF3b in low-resolution maps, it was important to be certain about their assignments in our current models. With our improved maps for the β-propeller bound near h14 and h44 on the 40S interface, we can unambiguously assign this density to the β-propeller of eIF3b, as it shows a better fit to the density compared to that of eIF3i (Llácer et al., 2015; Simonetti et al., 2016) since diameter of the inner and outer rims of the ring-shaped density are more appropriate for the size of a 9-bladed β-propeller (eIF3b) (Figures 2C and F) than to that of a 7-bladed β-propeller (eIF3i). Furthermore, density corresponding to loops present in the eIF3b and not in eIF3i is also observed (Figures 2D and 2E). Thus, we agree with (Simonetti et al., 2016) that the β-propeller of eIF3b instead of the β-propeller of eIF3i is bound near h14 and h44 in py48S-open-eIF3 and py48S-closed-eIF3 PICs. However, no density was observed at the GTPase binding site for the β-propeller of eIF3i (see below for eIF3i's position). Also, in these maps we do not observe density for the β-propeller of eIF3b at the solvent interface (Figure 1A, 1D). It is likely that our previously reported (py48S-open and py48S-closed) maps (Llácer et al., 2015) had a small fraction of 48S PIC particles with the eIF3b β-propeller in its more customary position at the solvent interface in addition to those harbouring this eIF3b domain at the subunit interface.

The eIF3b β-propeller is anchored between h14 and h44 using a loop (residues 387-400) and it is also in contact with h15 and ribosomal protein uS12 (Figures 2B, 2D). Although the β-propeller is positioned in proximity of eIF1A, no direct interaction between the two was observed. An eIF3b specific loop (residues 290 to 310) attached to β-propeller is observed in contact with domain III of eIF2γ in py48S-open-eIF3 and py48S-closed-eIF3 PICs (Figure 2E). The eIF3b RRM (RNA recognition motif) domain is also observed in py48S-open-eIF3 and

py48S-closed-eIF3 PICs (Figures 3A, 3B) and it interacts with h24 at the 40S platform, a long helix in the eIF3a C-terminal region (the same long helix is also in contact with the β-propeller of eIF3b), eIF1 and the eIF3c N-terminal tail (see below) (Figure 3C). Interaction of these eIF3 elements with the 40S and the other initiation factors eIF1 and eIF2 promotes a different conformation of the eIF3b/eIF3a-CTD subcomplex at the subunit interface compared to the same subcomplex bound at the 40S solvent interface (Figure 3D).

Trimeric complex of eIF3i-eIF3g-eIF3b C-terminal helix bound with eIF3b also re-locates to the subunit interface of 40S

The C-terminal helix of eIF3b was earlier shown to interact with the β-propeller of eIF3i (Erzberger et al., 2014; Herrmannova et al., 2012; des Georges et al., 2015; Valášek et al., 2017). Most of the residues in the helical linker region between this helix and the β-propeller of eIF3b are observed in py48S-open-eIF3 and py48S-closed-eIF3 PICs maps (Figures 2C, 2D, 2F, 3A and 3E). This helical linker region is in contact with h13 and h14 of rRNA (Figure 2D) and also with the previously mentioned C-terminal helix of eIF3a (Figure 3A). These interactions are similar to those occurring among the same eIF3 regions observed at the solvent interface in both mammalian 43S (des Georges et al., 2015; Valášek et al., 2017) and yeast py48S-5N maps (Figure 3D) (Llácer et al., 2018), suggesting that the interactions between the two β-propellers are intact at the solvent interface as well. Interestingly, at a lower resolution threshold of the maps, density for the trimeric complex eIF3i-eIF3g-eIF3b C-terminal helix can be observed attached to the eIF3b β-propeller in both py48S-open-eIF3 and py48S-closed-eIF3 PICs (Figures 2C and 3E). Thus, it appears that both β-propellers of eIF3b and eIF3i and the regions of eIF3g interacting with eIF3i move as a module to the subunit interface from the solvent interface. Also, the β-propeller of eIF3i appears to be flexible and not restricted to one conformation, resulting in weak density, and it does not contact the 40S. Finally, there is an unassigned density on the top of the β-propeller of eIF3b in contact with eIF2γ, which is larger and specially visible in py48S-closed-eIF3 (Figures 1A, 1D, 2C, 2F, 3A, 3B, 3E and S2), that might correspond to the RRM domain of eIF3g based on its size and proximity to eIF3i; although further studies are required to identify it with confidence.

N-terminal region of eIF3c bound on the subunit interface of 40S

Clear density is observed for different parts of the N-terminal region of eIF3c in py48S-open-eIF3 and py48S-closed-eIF3 PICs (Llácer et al., 2015). In our earlier studies we had observed a helical bundle of eIF3c on the subunit interface near h11/h24/h27. In the new py48S-open-eIF3 map, connectivity between the 5 helices can also be seen. Using our previous py48S-closed map (at slightly higher overall resolution, 4.9 Å), the newer py48S-open-eIF3 and py48S-closed-eIF3 maps simultaneously and aided by secondary structure predictions (Figure 4A) enabled us to model N-terminal region of eIF3c (numbers 117 to 226) in both py48S-open-eIF3 and py48S-closed-eIF3 maps, including some visible interacting rRNA side chains (Figure 4B, 4C and 4D). In our proposed model for these helices, most of the hydrophobic residues are buried and therefore protected from the solvent (Figure 4E), whereas charged residues are exposed and may interact with rRNA and other ribosomal proteins (Figure 4E and 4F). Also, a clear eIF3c density connecting the eIF3c helical bundle to eIF1 and eIF3b RRM is observed (Figures 3A, 3B, 3C, 4E and 4F), bridging eIF1 and eIF3b RRM. This might explain why, unlike the well-established eIF1:eIF3c-NTD interaction, a direct interaction of eIF1 with the eIF3b RRM has never been reported, as it might need a fragment of eIF3c to be stabilized. The bridging eIF3c density approaches the residues of eIF1 (50 – 56) that were earlier proposed (Reibarkh et al., 2008) to interact with eIF3c. The basic sidechains of eIF3c of residues 109 to 116 interact with h24 of the rRNA, while residues 98-107 that are acidic in nature interact with basic residues of eIF1 (see above), the RRM of eIF3b (around residues 145-154) and eL41 residues 19-23 (Figure 4E and 4F). Most of the observed residues involved in the contacts are highly conserved (Figure 4A). Additional density attached to eIF1 is observed and may correspond to the remaining N-terminal residues of eIF3c in both py48S-open-eIF3 and py48S-closed-eIF3 maps. However, further studies with better maps will be required to confirm this possibility. Furthermore, some extra density for the linker connecting this eIF3c helical bundle and its PCI domain (Figures 2A and 3A) is also observed.

C-terminal region of eIF3a bound on the subunit interface of 40S

A long helix of ~80 residues of the eIF3a C-terminal region is observed running alongside the β-propeller of eIF3b and interacting with both the face of the eIF3b RRM β-sheet and the eIF3b linker connecting the RRM to the β-propeller, thereby providing an additional connection between these two eIF3b domains in both maps (Figure 3A, 3B and 3C). The most N-terminal residues of this eIF3a helix run underneath the eIF3b β-propeller (Figures 3A and 3B) and also contact h14 and h44 of the 40S (Figure 3C) and the eIF3b helical linker that connects the eIF3b β-propeller to the eIF3b C-terminal helix that interacts with eIF3i (Figures 3A-C) (see above). However, the density is not clear enough to define unambiguously the side-chains of this eIF3a helix. A completely stretched linker of at least 110 amino acids would be needed to connect the eIF3a helix to the eIF3a PCI domain at the solvent side, a distance of more than 300 Å around the 40S (Figure 5A and 5B). Based on secondary structure predictions, sequence conservation among homologs, known biochemical information, and these distance constraints, we have tentatively assigned this linker to the 693-771 region at the eIF3a C-terminal end. Mutations in this region of eIF3a, including those for the KERR motif (Chiu et al., 2010; Khoshnevis et al., 2014) and/or substituting residues 692-701 with Ala (Szamecz et al., 2008), are known to impair the binding of eIF3a to the RRM of eIF3b and to the 40S ribosome, respectively. Finally, there is an unassigned density at the extreme C-terminus of the eIF3a helix that also approaches eIF2γ, which probably belongs to eIF3a, but the low resolution of this density and the fact that there are still some segments of factors not accounted for, prevents us from an assigning this density unambiguously (Figures 1D, 3B, and S2D).

mRNA path in 48S

Since a longer mRNA was used to reconstitute py48S-open-eIF3 PIC compared to the previous py48S-open, mRNA density is observed at the openings of both the entry and exit portions of the mRNA-binding channel on the 40S (Figure 1). However, there is no distinct high-resolution mRNA density throughout the channel outside of the P site. A stretch of 3 nucleotides of mRNA have been modelled with confidence at the P site, compared to 2 nucleotides in the previous py48S-open complex. The AU of the codon positions 1 and 2 are observed interacting with the UA of the anticodon of the tRNAi (Figure S3). There is no distinct density for C at position 3 of the AUC codon, probably due to the mismatch in codon:anticodon base-pairing. An additional

nucleotide A at the -1 position of mRNA is observed in this map (Figure S3). Thus, overall the mRNA seems to have minimal interaction with the widened mRNA channel of the 40S subunit in this open conformation of the 48S PIC.

Concluding remarks.

The structures of py48S-open-eIF3 PIC and py48S-closed-eIF3 presented here show the interactions of the β-propeller and RRM of eIF3b at the subunit interface. eIF3 adopts a similar conformation in both complexes, and the only differences found between them are the consequences of the rearrangement of eIF3b needed to maintain the same set of interactions with mobile elements, including eIF2γ and eIF1, whose position is slightly different in the open vs. closed states (Figure 5C). eIF3i is also resolved (especially in the py48S-closed-eIF3 map) along with eIF3b in the new structures, however, its β-propeller is weakly attached to eIF3b and does not make any direct contacts with the 40S subunit. This stands in contrast to a model proposed recently for the rearrangement of eIF3 during translation initiation wherein the β-propellers of eIF3b and eIF3i re-locate independently to the subunit interface at different stages of the process (Simonetti et al., 2016). This model was based on a model of a mammalian 48S late stage IC in which the β-propeller of eIF3i was positioned at the GTPase binding site on the subunit interface (Simonetti et al., 2016). However, as this density was later re-interpreted as ABCE1 protein (Mancera-Martínez et al., 2017), the model of structural rearrangements of eIF3 during initiation wherein the β-propellers of eIF3b and eIF3i independently move to the subunit interface during different steps (Simonetti et al., 2016) now seems unlikely. Instead, we propose an alternative model in which the β-propellers of eIF3b and eIF3i re-locate together from the solvent interface to the subunit interface after mRNA binding or early stages of codon:anticodon recognition, with only the eIF3b propeller contacting the 40S subunit in both states, and thereafter these domains relocate back to their original position after the release of eIF1 and its replacement by the eIF5 N-terminal domain at the subunit interface (Llácer et al., 2018) (Figure 6).

eIF3 is involved in nearly all the steps of initiation, including the stimulation of the binding of eIF2 TC and other eIFs to the 40S ribosomal subunit; the attachment of the 43S complex to mRNA; the subsequent scanning along mRNA to reach the start AUG codon; and finally,

prevention of the joining of small and large ribosomal subunits prior to start codon recognition (Hinnebusch, 2014; Hinnebusch, 2017; Valášek et al., 2017). However, little is known about the details of function of eIF3 and role of each subunit for these activities. Moreover, there is no understanding of the role of eIF3 especially in the conformation where some of its peripheral subunits are positioned on the inter-subunit interface, as observed in the PICs in this study. Based on the models of eIF3 presented here, it appears that interactions of the eIF3b propeller with eIF2γ at the subunit interface may contribute to anchoring TC to the PIC prior to AUG recognition, Pi release, and dissociation of eIF2-GDP. Similarly, the bridging of eIF3b RRM-eIF1 association by segments of the eIF3c-NTD butressed by a segment of the eIF3a-CTD could be important to anchor eIF1 on the scanning PIC and prevent its unscheduled dissociation at non-AUG codons. Accordingly, eIF1 dissociation and loss of its network of interactions with the 3b-RRM and eIF3c would precipitate the re-location of the eIF3 b-i-g module back to the solvent side of the 40S, and that re-location of the eIF3 b-i-g module would be a prerequisite for the eIF5-NTD binding to the platform as observed in (Llácer et al., 2018) and its attendant adjustment of tRNAi deeper in the P site that sets the stage for the final stages of initiation.

MATERIALS & METHODS

Reconstitution of the 48S complex

Kluyveromyces lactis 40S subunits were prepared as described earlier (Fernandez et al., 2014). *Saccharomyces cerevisiae* eIF2 was expressed in yeast while eIF1, eIF1A, eIF5, eIF4A, eIF4B and the complex eIF4G1:eIF4E were expressed in *Escherichia coli* as recombinant proteins and purified as described (Acker et al., 2007) (Mitchell et al., 2010) (Llácer et al., 2018) . eIF3 was also expressed in yeast as previously described (Acker et al., 2007) but with modifications to avoid eIF5 contamination. To achieve that we replaced the phosphocellulose column step of the reported eIF3 purification, by a Q-sepharose column step and a very long elution KCl gradient from 100 mM to 1M (50 columns), obtaining two batches of eIF3, one without eIF5, the other enriched in eIF5. Wild type $tRNA_i$ was overexpressed and purified from yeast and aminoacylated as described (Acker et al., 2007). The mRNA expression construct comprised a T7 promoter followed by the 49-nt unstructured mRNA sequence of 5′-GGG$[CU]_3[UC]_4$UAACUAUAAAA<u>AUC</u>$[UC]_2$UUC$[UC]_4$GAU-3′ (with start codon underlined), cloned between XhoI and NcoI sites in a pEX-A2 plasmid (Eurofins Genomics).
First, a 43S mix was reconstituted by incubating 40S with eIF1, eIF1A, TC (consisting of eIF2, GDPCP and Met-$tRNA_i$), and eIF3 in 40S:eIF1:eIF1A:TC:eIF3 molar ratios of 1:2.5:2.5:2:2, in 20 mM MES, pH 6.5, 80 mM potassium acetate, 10 mM ammonium acetate, 5-8mM magnesium acetate, 2mM dithiothreitol (DTT), 1 μM zinc acetate.

Separately, an mRNA-eIF4 complex was prepared, containing eIF4G1, eIF4E, eIF4A, eIF4B and capped mRNA in molar ratios of 1.5:1.5:5:2:2.5 with respect to the 40S ribosome, in 20 mM Hepes, pH 7.4, 100 mM potassium chloride, 5mM magnesium chloride, 2mM DTT, 3mM AMPPNP). The volume of the mRNA-eIF4 mix was 5 times smaller than the 43S mix volume. Both the 43S mix and the mRNA-eIF4 mix were incubated separately for 5 min at room temperature before mixing them. After incubation for 2 min at room temperature, the sample (at a 40S concentration of 80 nM) was cooled to 4°C and used immediately to make cryo-EM grids without further purification.

Electron microscopy

Three µl of the 48S complex was applied to glow-discharged Quantifoil R2/2 cryo-EM grids covered with continuous carbon (of ~50Å thick) at 4 °C and 100% ambient humidity. After 30s incubation, the grids were blotted for 2.5-3 s and vitrified in liquid ethane using a Vitrobot Mk3 (FEI). Automated data acquisition was done using the EPU software (FEI) on a Titan Krios microscope operated at 300 kV under low-dose conditions (30 e-/Å2) using a defocus range of 1.2 – 3.2 µm. Images of 1.1 s/exposure and 34 movie frames were recorded on a Falcon III direct electron detector (FEI) at a calibrated magnification of 104,478 (yielding a pixel size of 1.34 Å). Micrographs that showed noticeable signs of astigmatism or drift were discarded.

Analysis and structure determination

The movie frames were aligned with MOTIONCORR (Li et al., 2013) for whole-image motion correction. Contrast transfer function parameters for the micrographs were estimated using Gctf (Zhang, 2016). Particles were picked using RELION (Scheres, 2012). References for template-based particle picking (Scheres, 2015) were obtained from 2D class averages that were calculated from particles picked with EMAN2 (Tang et al., 2007) from a subset of the micrographs. 2D class averaging, 3D classification and refinements were done using RELION-1.4 (Scheres, 2012). Both movie processing (Bai et al., 2013) in RELION-1.4 and particle ‘‘polishing’’ was performed for all selected particles for 3D refinement. Resolutions reported here are based on the gold-standard FSC = 0.143 criterion (Scheres and Chen, 2012). All maps were further processed for the modulation transfer function of the detector, and sharpened (Rosenthal and Henderson, 2003). Local resolution was estimated using Relion and ResMap (Kucukelbir et al., 2014).

For 48S-open-eIF3 dataset 2610 images were recorded from two independent data acquisition sessions. An initial reconstruction was made from all selected particles (360,729) after 2D class averaging using the yeast 40S crystal structure (PDB: 4V88) low-pass filtered to 60 Å as an initial model. Next, a 3D classification into 12 classes with fine angular sampling and local searches was performed to remove bad particles/empty 40S particles from the data. Three highly populated classes (144,292 particles) showed density for the TC. Then we performed two

consecutive masked 3D classifications with subtraction of the residual signal (Bai et al., 2015), by creating masks around the density attributed to the TC and to the different domains of eIF3 at the subunit interface. In the first 'focused' 3D classification using the TC mask we isolated 104,792 particles containing a distinct density for the TC. In the second round of 'focused' 3D classification using the eIF3 mask, only 1 class contained eIF3 in high occupancy (13,038 particles, 2.6 % of the total, 4.6Å). The latter class was further classified in two different classes: a) A 48S in a partially open form (7,288 particles; 5.6Å), where the head of the 40S adopts an intermediate position in between that in the closed and open forms. b) the other class is in the fully open form (5,750 particles, 5.15Å) which is conformationally identical to our previously reported py48S-open. The quality of the density for eIF3 at the subunit interface is better in the latter class than that in the partially open form or the one resulted from the combination of the two classes.

We have also reprocessed our previous dataset of the py48S-closed conformation by using the image processing tools that were not available at the time we published our previous work with the aim of improving the local resolution of eIF3 at the subunit interface by isolating a larger number of particles containing higher occupancy for eIF3. We started with more than 1,182,000 particles after 2D-classification and after an initial reconstruction done with all selected particles, a first attempt of focused classification with subtraction of the residual signal using a mask around the observed eIF3 beta propeller near the TC did not yield a satisfactory result. Instead, we carried out a conventional 3D-classification in 16 classes and selected the classes containing a clear density for the TC (365,343) followed by movie-processing/particle polishing. Then we performed three consecutive masked 3D classifications with subtraction of the residual signal, by using masks around the density attributed to the eIF3 beta propeller near the TC (selecting 1 class out of four, 128,915 particles), around the tRNA/alpha subunit of eIF2 (selecting 3 classes out of five, 55,915 particles) and around all the different domains of eIF3 at the subunit interface. In this latter classification we obtained three different classes in which only one of them (12,586 particles, 5.75Å) showed a very disctinct an unambiguous density for all the eIF3 subunits, reflecting the higher mobility and flexibility of all these eIF3 domains.

Model building and refinement

The atomic model of py48S in open conformation (PDB: 3JAQ) was placed into density by rigid-body fitting using Chimera (Pettersen et al., 2004). Overall densities for eIF3 at the subunit interface were similar in both the open and closed structures, so model building for eIF3 was done simultaneously in both maps, using one or another depending on the quality of the map for each of the different domains of eIF3. Initially, all the different domains of eIF3 were fitted by rigid-body using Chimera as follows:

a) The eIF3a/eIF3c PCI dimer was taken from the PDB:3JAP and placed in its corresponding density at the solvent side of the 40S in the 48S-open-eIF3 map.

b) eIF3b β-propeller was taken from the PDB:4NOX and placed into the drum-like density below the TC, in almost the same orientation to that found in the PDB:5K1H.

c) The ternary complex eIF3i/eIF3g/eIF3b-cterm originally placed into the above mentioned drum-like density was now placed (together with the helical linker connecting the eIF3b β-propeller with its c-terminal helix in contact with eIF3i) into the low-resolution density in close contact with the eIF3b β-propeller, therefore adopting the two beta propellers a rather similar arrangement to that found at the solvent side of the 40S (Llácer et al., 2018).

d) eIF3b RRM and the linker connecting it with the eIF3b β-propeller were taken from PDB:5K1H, and almost placed identically, with minor changes (see below).

e) eIF3a c-term helix in contact with eIF3b and the eIF3c helical bundle were not displaced from its original position.

Then, each domain of eIF3 was rigid-body fitted in Coot (Emsley et al., 2010) and further model building was also done in Coot v0.8. This further model building included for example:

1) The replacement of each amino acid of eIF3b to its corresponding counterpart in *S. cerevisiae*

2) eIF3a C-term helix model building. Possible residue numbering for eIF3a C-term helix was based on eIF3a secondary structure predictions (consensus of programs PSSPred, SOPMA, Jpred), sequence conservation among homologs (alignment done in Clustal Omega using *S. cerevisiae, H. sapiens, A. thaliana, C. elegans, D. melanogaster, S. pombe* sequences; we expect a higher conservation in regions of eIF3a involved in interactions), distance restraints between this helix and the PCI domain of eIF3a at the solvent side (taking also into account sequence conservation in different organisms) and known interactions with eIF3b and the eIF3b RRM domain (Chiu et al., 2010) and with the ribosome (Szamecz et al., 2008). We decided to keep the

poly-alanine sequence found in the original model since this is still a tentative sequence assignment done in a low-resolution map.

3) eIF3c N-term model building: For the 5-helical bundle model building we have used blurred maps of our previous py48S-closed model. Length of the helices matched the lengths predicted by secondary structure prediction programs and the newer improved maps helped to model the connection between helices, aided by the fact that the extra density connecting the helical-bundle with eIF1/RRM and the PCI helped identifying the N- and C-terminus, respectively, of the helical-bundle. Density for some bulky side chains also helped in the sequence assignment as well as sequence conservation among homologs (alignment using *S. cerevisiae, H. sapiens, A. thaliana, D rerio, D. melanogaster, S. pombe* sequences; residues of eIF3c involved in interactions is expected to be more conserved).

Model refinement was carried out in Refmac v5.8 optimized for electron microscopy (Brown et al., 2015), using external restraints generated by ProSMART and LIBG (Brown et al., 2015). Average FSC was monitored during refinement. The final model was validated using MolProbity (Chen et al., 2010). Cross-validation against overfitting was calculated as previously described (Brown et al., 2015; Amunts et al., 2014). All figures were generated using PyMOL (DeLano, 2006) Coot or Chimera.

Data Resources

Two maps have been deposited in the EMDB with accession codes EMDB: 0057 and EMDB: 0058, for the py48S-open-eIF3 and py48S-closed-eIF3 maps, respectively. Two atomic coordinate models have been deposited in the PDB with accession codes PDB: 6GSM and PDB: 6GSN, for the py48S-open-eIF3 and py48S-closed-eIF3 models, respectively. These models replace previous PDB:3JAQ and PDB:3JAP models (Llácer et al., 2015) and are also linked to previous published maps EMDB: 3050 and EMDB: 3049, respectively (Llácer et al., 2015).

Figure Legends

Figure 1. Cryo-EM structure of 48S-open-eIF3 and 48S-closed-eIF3

(A) Cryo-EM maps of the 48S-open-eIF3 PIC shown in two orientations. Regions of the map are colored by component to show the 40S subunit (yellow), eIF1A (blue), eIF1 (cyan), Met-$tRNA_i^{Met}$ (green), mRNA (magenta), eIF2α (violet), eIF2γ (orange), eIF2β (red), eIF3 (different shades of pink). The 40S head is shown in a darker yellow compared to the body. The same colors are used in all the figures.

(B) Gold-standard Fourier Shell Correlation (FSC) curves for the 48S-open-eIF3 and 48S-closed-eIF3 maps.

(C) eIF1 N-terminal tail (transparent cyan surface) approaching and making contacts with eIF2γ

(D) Cryo-EM maps of the py48S-closed-eIF3 PIC shown in two orientations.

Figure 2. Contacts of eIF3 PCI and of eIF3b-β propeller with the other components in the 48S PIC.

(A) Fitting of the eIF3a/c PCI domain dimer in 48S-open-eIF3 map. Inset: Superimposition of the PCIs in the open/closed maps.

(B) View of the contacts of the eIF3b β-propeller with different parts of the 40S subunit (colored differently), eIF2γ and eIF3a-CTD.

(C) Fitting of eIF3b and eIF3i β-propellers in 48S-closed-eIF3 map.

(D,E) Fitting of some well-resolved loops of the eIF3b β-propeller in the 48S-closed-eIF3 map.

(F) Fitting of eIF3b and eIF3i β-propellers in 48S-open-eIF3 map.

Figure 3. Contacts of eIF3b, eIF3a C-term and eIF3c N-term with the other components in the 48S PIC.

(A) Fitting of all eIF3b, eIF3a C-term and eIF3c N-term in 48S-open-eIF3 map.

(B) As in A, fitting of all eIF3b, eIF3a C-term and eIF3c N-term in 48S-closed-eIF3 map.

(C) View of the contacts of the eIF3b β-propeller, eIF3b RRM domain, eIF3a-CTD and the most N-terminal of eIF3c between them and with different parts of the 40S subunit (colored differently), eIF2γ and eIF1

(D) Superimposition of the eIF3b/eIF3i/eIF3g/eIF3a-Cterm quaternary complex observed in 48S-closed-eIF3 with that found on the 40S solvent side in py48S-eIF5N (in grey; PDB: 6FYY), aligning the eIF3b β-propellers, shows how this eIF3 subcomplex undergoes internal rearrangements in the transition between the two states, possibly resulting from constraints imposed by its interactions with eIF2 and eIF1 unique to the subunit interface location.

(E) Fitting of the eIF3b and eIF3i β-propellers in the 48S-closed-eIF3 map in a different view to that in Figure 3C to highlight the fitting of the eIF3b helical linker connecting the two different eIF3 β-propellers.

Figure 4. Proposed model for the N-terminal region of eIF3c and its contacts with the other components in the 48S PIC.

(A) Amino acid sequence, secondary structure prediction and residue conservation of the eIF3c N-terminal region. The β-strands and α-helices are depicted as arrows and rectangles, respectively. Yellow rectangles account for the consensus between the three programs used for secondary structure prediction (see Methods section), whereas those in white correspond to the prediction of at least two of these programs. Residues shown in red are identical in a multiple sequence alignment (see Methods section) whereas similar residues are in blue.

(B,C) Two different views of the eIF3c 5-helical bundle showing the connectivity between the five helices. Residue numbers at the beginning and end of each helix are labeled, highlighting

that there is hardly any discrepancy between the model and the secondary structure prediction shown in A.

(D) A few side chains are seen, especially those in close contact with rRNA. Two very conserved basic residues (R201, K204) interacting with h11 are labeled.

(E,F) Surface electrostatic representation of 40S proteins and of eIF1 and eIF3b RRM domain and cartoon representation of rRNA and of eIF3c N-terminal region. The C_β for each residue with hydrophobic, basic and acidic sidechains of eIF3c is represented as white, blue and red spheres, respectively. Residue numbers at the beginning and end of each helix are also labeled here. In E, we can see that most of the hydrophobic residues are buried, whereas in E and F we can see that basic residues are exposed and would interact mainly with rRNA and acidic residues would interact with the basic surfaces of eIF1 and eIF3b RRM and of eL41 and uS15.

Figure 5. eIF3a C-terminal helix modeling

(A) Amino acid sequence, secondary structure prediction and residue conservation of the eIF3a C-terminal region. As in figure 4A, β-strands and α-helices are depicted as arrows and rectangles, respectively. Yellow rectangles account for the consensus between the three programs used for secondary structure prediction (see Methods section), whereas those in white correspond to the prediction of at least two of these programs. Residues shown in red are identical in a multiple sequence alignment (see Methods section) whereas similar residues are in blue.

(B) Proposed path along the solvent side of the 40S for the central part of eIF3a connecting the eIF3a/PCI domain and eIF3a C-term helix. A linker of more than 300 Å-distance is needed to connect the C-end of the PCI domain with the N-end of the eIF3a C-terminal helix that interacts

with eIF3b. A semitransparent cartoon representation of the eIF3b/3i/3g/3a-Cterm complex when this resides on the solvent-exposed side of the 40S subunit is also shown to illustrate that the re-location of eIF3b/3i/3g/3a-Cterm to the 40S subunit interface is probably accomplished by stretching this central eIF3a linker.

(C) Superimposition of eIF3 in the 48S-closed-eIF3 and 48S-open-eIF3 structures, by aligning the 40S bodies in both structures. For clarity, eIF3i/eiF3g subunits are not shown. tRNAi, eIF2 and eIF1 are shown as surfaces. Different components from 48S-closed-eIF3 structure are colored gray.

Figure 6. β-propellers repositioning after AUG recognition

(A,B) Side and top views of a composite representation showing the two different locations reported for the quaternary complex eIF3b/eIF3i/eIF3g/eIF3a-Cterm on the subunit or solvent surfaces of the 40S subunits in py48S-closed-eIF3 and py48S-eIF5N (Llácer et al., 2018). The arrow shows the direction of the rearrangement of this eIF3 subcomplex from the interface to solvent surface, which probably occurs after AUG recognition, complete accommodation of $tRNA_i$ and eIF1 dissociation from the 48S.

Supplementary Figures:

Figure S1. Scheme of 3D classification of data

For 48S-open-eIF3 360,729 particles were selected after 2D classification and an initial 3D refinement was done. After a 3D-classification in twelve classes, three classes contained clear

density for TC and were grouped together. Then focused 3D classifications were carried out, using separately a 'TC mask' first and then an 'eIF3 mask' (shown by an outline). As a result, we obtained a class with high occupancy for eIF3 at the subunit interface (13,038 particles) that could be further classified into two classes showing a different degree of head tilting. One of them corresponds to the fully open head conformation (48S-open-eIF3, 5,750 particles, 5.15 Å) Previous py48S-closed dataset was reprocessed. 1,182,041 particles were selected after 2D classification and an initial 3D refinement was done. After a 3D-classification in sixteen classes, four classes contained clear density for TC and were joined together. Then focused 3D classifications were carried out. The eIF3 masks 'bgi mask' and 'eIF3 mask' as well as the 'tRNA/alpha mask' used separately for focused 3D classification are shown by an outline. A final class of 12,586 particles showing higher occupancy for eIF3 was obtained. See 'Analysis and structure determination' section for detailed information.

Figure S2. Map quality and local resolution

Surface (left or top) and cross-sections (right or bottom) of gaussian-filtered maps, colored according to local resolution.

(A) 48S-open-eIF3, front view

(B) 48S-open-eIF3, lateral view

(C) 48S-closed-eIF3, front view

(D) 48S-closed-eIF3, lateral view

Figure S3. P-site conformation

Detailed view of the codon-anticodon area on py48S-open-eIF3. There is only density for the two first bases of the codon A(+1) and U(+2) and the preceding base A(-1).

References

Acker, M. G., Kolitz, S. E., Mitchell, S. F., Nanda, J. S., and Lorsch, J. R. (2007). Reconstitution of yeast translation initiation. Methods Enzymol *430*, 111-145.

Amunts, A., Brown, A., Bai, X. C., Llacer, J. L., Hussain, T., Emsley, P., Long, F., Murshudov, G., Scheres, S. H., and Ramakrishnan, V. (2014). Structure of the yeast mitochondrial large ribosomal subunit. Science *343*, 1485-1489.

Aylett, C. H., and Ban, N. (2017). Eukaryotic aspects of translation initiation brought into focus. Philos Trans R Soc Lond B Biol Sci *372*,

Bai, X. C., Fernandez, I. S., McMullan, G., and Scheres, S. H. (2013). Ribosome structures to near-atomic resolution from thirty thousand cryo-EM particles. Elife *2*, e00461.

Bai, X. C., Rajendra, E., Yang, G., Shi, Y., and Scheres, S. H. (2015). Sampling the conformational space of the catalytic subunit of human γ-secretase. Elife *4*,

Brown, A., Long, F., Nicholls, R. A., Toots, J., Emsley, P., and Murshudov, G. (2015). Tools for macromolecular model building and refinement into electron cryo-microscopy reconstructions. Acta Crystallogr D Biol Crystallogr *71*, 136-153.

Chen, V. B., Arendall, W. B., Headd, J. J., Keedy, D. A., Immormino, R. M., Kapral, G. J., Murray, L. W., Richardson, J. S., and Richardson, D. C. (2010). MolProbity: all-atom structure validation for macromolecular crystallography. Acta Crystallogr D Biol Crystallogr *66*, 12-21.

Chiu, W. L., Wagner, S., Herrmannova, A., Burela, L., Zhang, F., Saini, A. K., Valasek, L., and Hinnebusch, A. G. (2010). The C-terminal region of eukaryotic translation initiation factor 3a (eIF3a) promotes mRNA recruitment, scanning, and, together with eIF3j and the eIF3b RNA recognition motif, selection of AUG start codons. Mol Cell Biol *30*, 4415-4434.

DeLano, W. L. (2006). The PyMOL Molecular Graphics System. http://www.pymol.org

des Georges, A., Dhote, V., Kuhn, L., Hellen, C. U., Pestova, T. V., Frank, J., and Hashem, Y. (2015). Structure of mammalian eIF3 in the context of the 43S preinitiation complex. Nature *525*, 491-495.

Emsley, P., Lohkamp, B., Scott, W. G., and Cowtan, K. (2010). Features and development of Coot. Acta Crystallogr D Biol Crystallogr *66*, 486-501.

Erzberger, J. P., Stengel, F., Pellarin, R., Zhang, S., Schaefer, T., Aylett, C. H., Cimermancic, P., Boehringer, D., Sali, A., Aebersold, R., and Ban, N. (2014). Molecular architecture of the 40SeIF1eIF3 translation initiation complex. Cell *158*, 1123-1135.

Fernandez, I. S., Bai, X. C., Murshudov, G., Scheres, S. H., and Ramakrishnan, V. (2014). Initiation of translation by cricket paralysis virus IRES requires its translocation in the ribosome. Cell *157*, 823-831.

Herrmannova, A., Daujotyte, D., Yang, J. C., Cuchalova, L., Gorrec, F., Wagner, S., Danyi, I., Lukavsky, P. J., and Valasek, L. S. (2012). Structural analysis of an eIF3 subcomplex reveals conserved interactions required for a stable and proper translation pre-initiation complex assembly. Nucleic Acids Res *40*, 2294-2311.

Heuer, A., Gerovac, M., Schmidt, C., Trowitzsch, S., Preis, A., Kötter, P., Berninghausen, O., Becker, T., Beckmann, R., and Tampé, R. (2017). Structure of the 40S-ABCE1 post-splitting complex in ribosome recycling and translation initiation. Nat Struct Mol Biol *24*, 453-460.

Hinnebusch, A. G. (2014). The scanning mechanism of eukaryotic translation initiation. Annu Rev Biochem *83*, 779-812.

Hinnebusch, A. G. (2017). Structural Insights into the Mechanism of Scanning and Start Codon Recognition in Eukaryotic Translation Initiation. Trends Biochem Sci *42*, 589-611.

Khoshnevis, S., Gunišová, S., Vlčková, V., Kouba, T., Neumann, P., Beznosková, P., Ficner, R., and Valášek, L. S. (2014). Structural integrity of the PCI domain of eIF3a/TIF32 is required for mRNA recruitment to the 43S pre-initiation complexes. Nucleic Acids Res *42*, 4123-4139.

Kucukelbir, A., Sigworth, F. J., and Tagare, H. D. (2014). Quantifying the local resolution of cryo-EM density maps. Nat Methods *11*, 63-65.

Li, X., Mooney, P., Zheng, S., Booth, C. R., Braunfeld, M. B., Gubbens, S., Agard, D. A., and Cheng, Y. (2013). Electron counting and beam-induced motion correction enable near-atomic-resolution single-particle cryo-EM. Nat Methods *10*, 584-590.

Llácer, J. L., Hussain, T., Marler, L., Aitken, C. E., Thakur, A., Lorsch, J. R., Hinnebusch, A. G., and Ramakrishnan, V. (2015). Conformational Differences between Open and Closed States of the Eukaryotic Translation Initiation Complex. Mol Cell *59*, 399-412.

Llácer, J. L., Hussain, T., Saini, A. K., Nanda, J. D., Kaur, S., Gordiyenko, Y., Kumar, R., Hinnebusch, A. G., Lorsch, J. R., and Ramakrishnan, V. (2018). Translational initiation factor eIF5 replaces eIF1 on the 40S ribosomal subunit to promote start-codon recognition. bioRxiv

Mancera-Martínez, E., Brito Querido, J., Valasek, L. S., Simonetti, A., and Hashem, Y. (2017). ABCE1: A special factor that orchestrates translation at the crossroad between recycling and initiation. RNA Biol 1-7.

Mitchell, S. F., Walker, S. E., Algire, M. A., Park, E. H., Hinnebusch, A. G., and Lorsch, J. R. (2010). The 5'-7-methylguanosine cap on eukaryotic mRNAs serves both to stimulate canonical translation initiation and to block an alternative pathway. Mol Cell *39*, 950-962.

Pettersen, E. F., Goddard, T. D., Huang, C. C., Couch, G. S., Greenblatt, D. M., Meng, E. C., and Ferrin, T. E. (2004). UCSF Chimera--a visualization system for exploratory research and analysis. J Comput Chem *25*, 1605-1612.

Reibarkh, M., Yamamoto, Y., Singh, C. R., del Rio, F., Fahmy, A., Lee, B., Luna, R. E., Ii, M., Wagner, G., and Asano, K. (2008). Eukaryotic initiation factor (eIF) 1 carries two distinct eIF5-binding faces important for multifactor assembly and AUG selection. J Biol Chem *283*, 1094-1103.

Rosenthal, P. B., and Henderson, R. (2003). Optimal determination of particle orientation, absolute hand, and contrast loss in single-particle electron cryomicroscopy. J Mol Biol *333*, 721-745.

Scheres, S. H. (2012). RELION: implementation of a Bayesian approach to cryo-EM structure determination. J Struct Biol *180*, 519-530.

Scheres, S. H. (2015). Semi-automated selection of cryo-EM particles in RELION-1.3. J Struct Biol *189*, 114-122.

Scheres, S. H., and Chen, S. (2012). Prevention of overfitting in cryo-EM structure determination. Nat Methods *9*, 853-854.

Simonetti, A., Brito Querido, J., Myasnikov, A. G., Mancera-Martinez, E., Renaud, A., Kuhn, L., and Hashem, Y. (2016). eIF3 Peripheral Subunits Rearrangement after mRNA Binding and Start-Codon Recognition. Mol Cell *63*, 206-217.

Szamecz, B., Rutkai, E., Cuchalová, L., Munzarová, V., Herrmannová, A., Nielsen, K. H., Burela, L., Hinnebusch, A. G., and Valásek, L. (2008). eIF3a cooperates with sequences 5' of uORF1 to promote resumption of scanning by post-termination ribosomes for reinitiation on GCN4 mRNA. Genes Dev *22*, 2414-2425.

Tang, G., Peng, L., Baldwin, P. R., Mann, D. S., Jiang, W., Rees, I., and Ludtke, S. J. (2007). EMAN2: an extensible image processing suite for electron microscopy. J Struct Biol *157*, 38-46.

Valášek, L. S., Zeman, J., Wagner, S., Beznosková, P., Pavlíková, Z., Mohammad, M. P., Hronová, V., Herrmannová, A., Hashem, Y., and Gunišová, S. (2017). Embraced by eIF3:

structural and functional insights into the roles of eIF3 across the translation cycle. Nucleic Acids Res

Zhang, K. (2016). Gctf: Real-time CTF determination and correction. J Struct Biol *193*, 1-12.

Figure 1

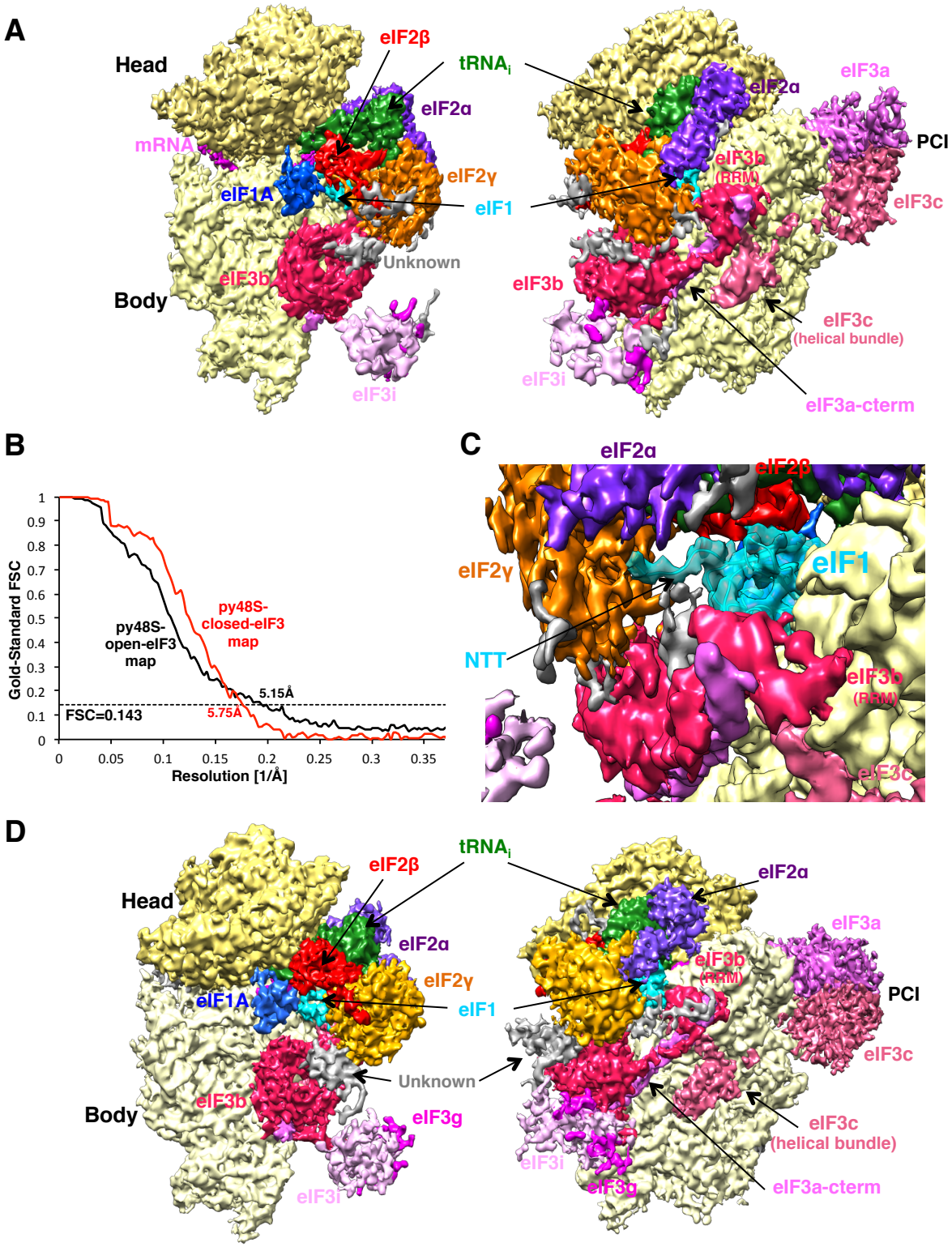

Figure 2

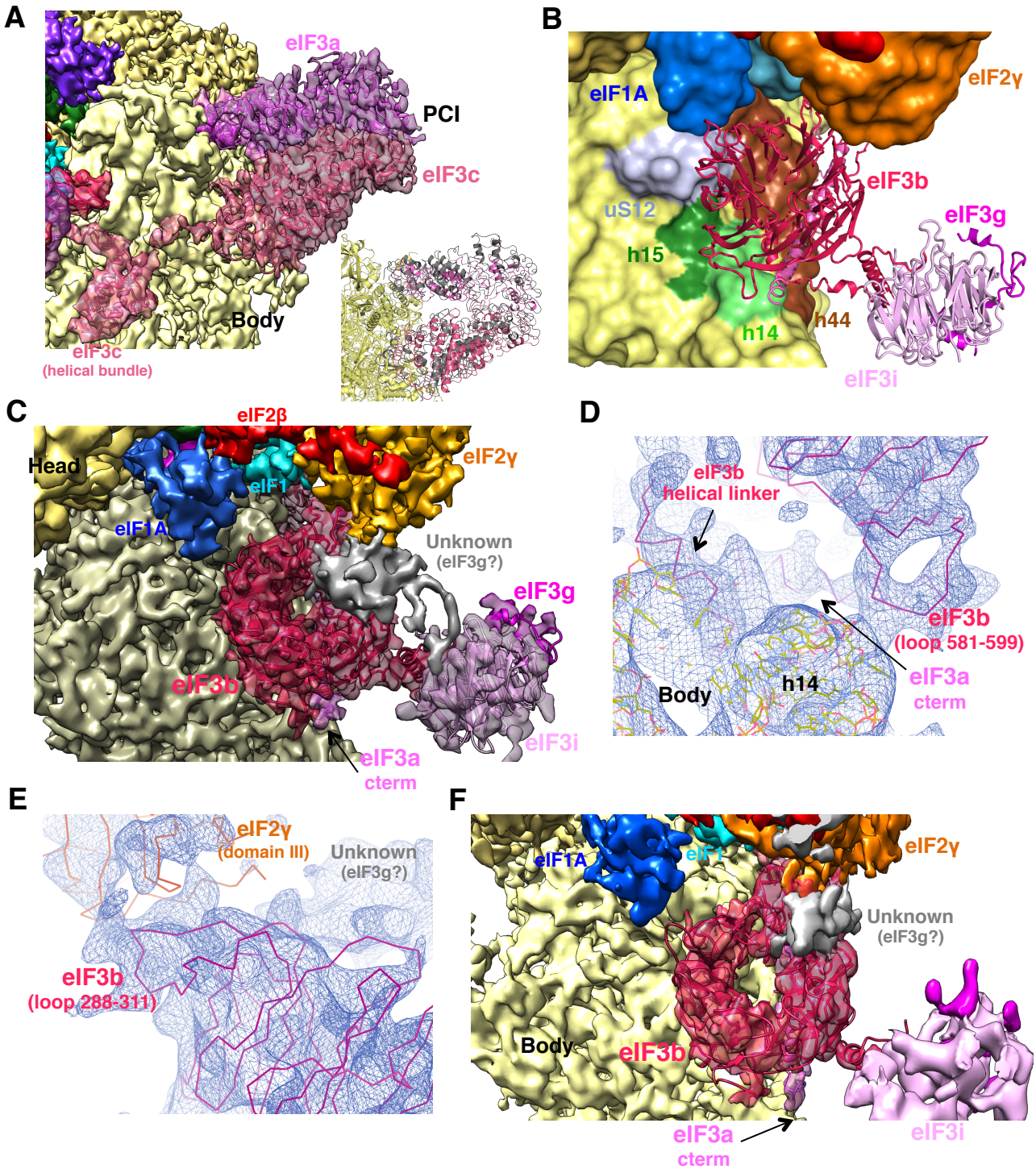

Figure 3

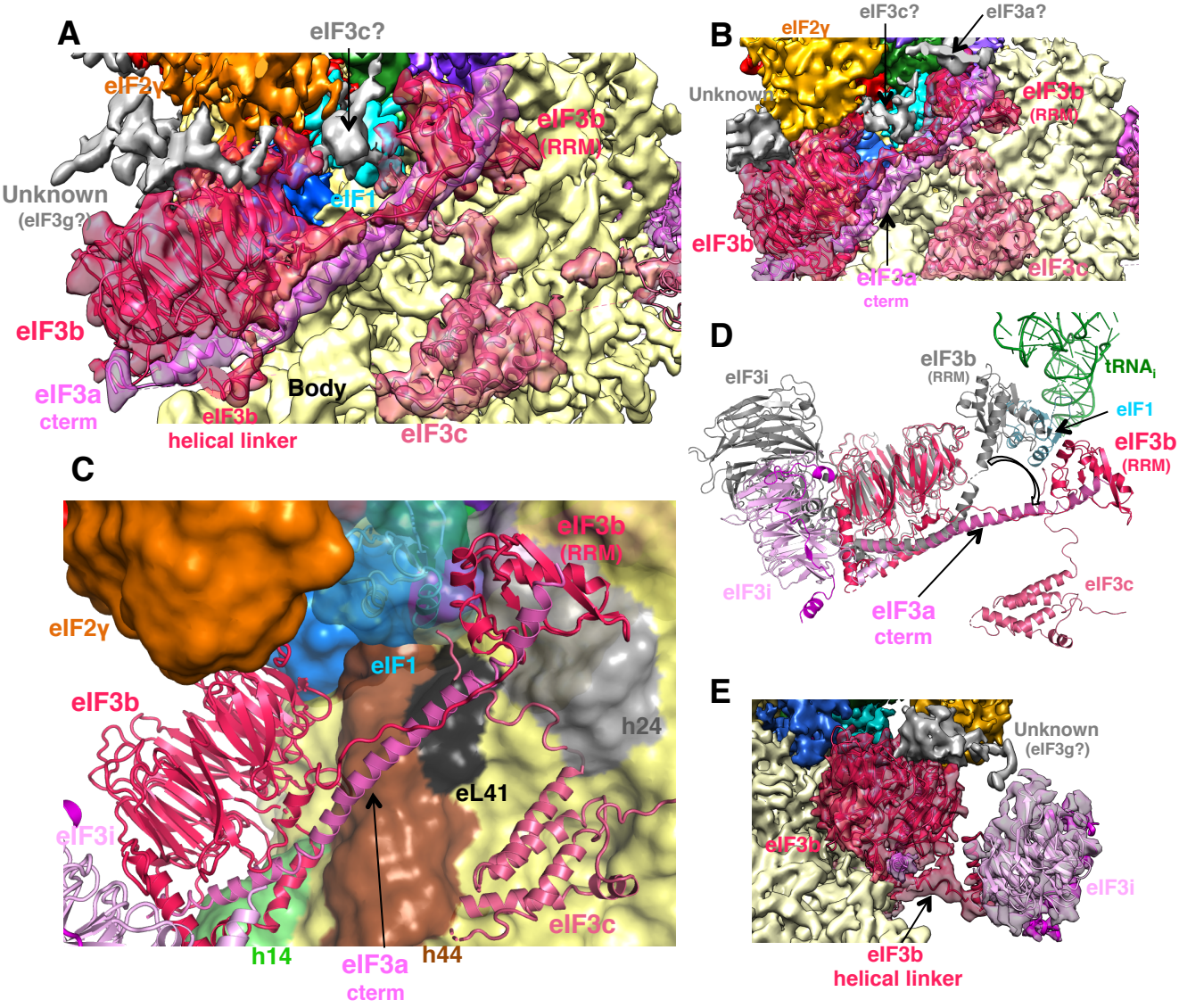

Figure 4

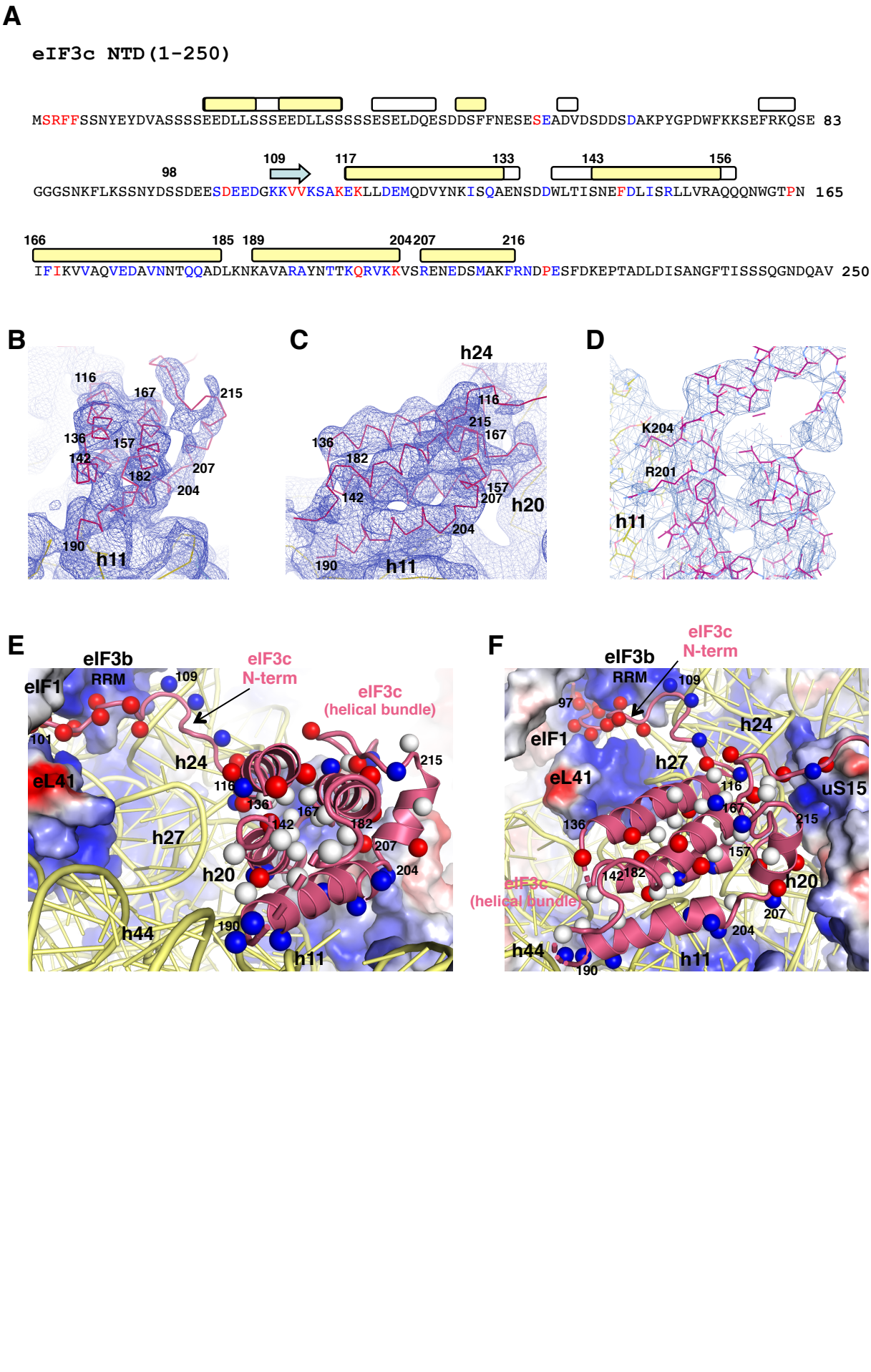

Figure 5

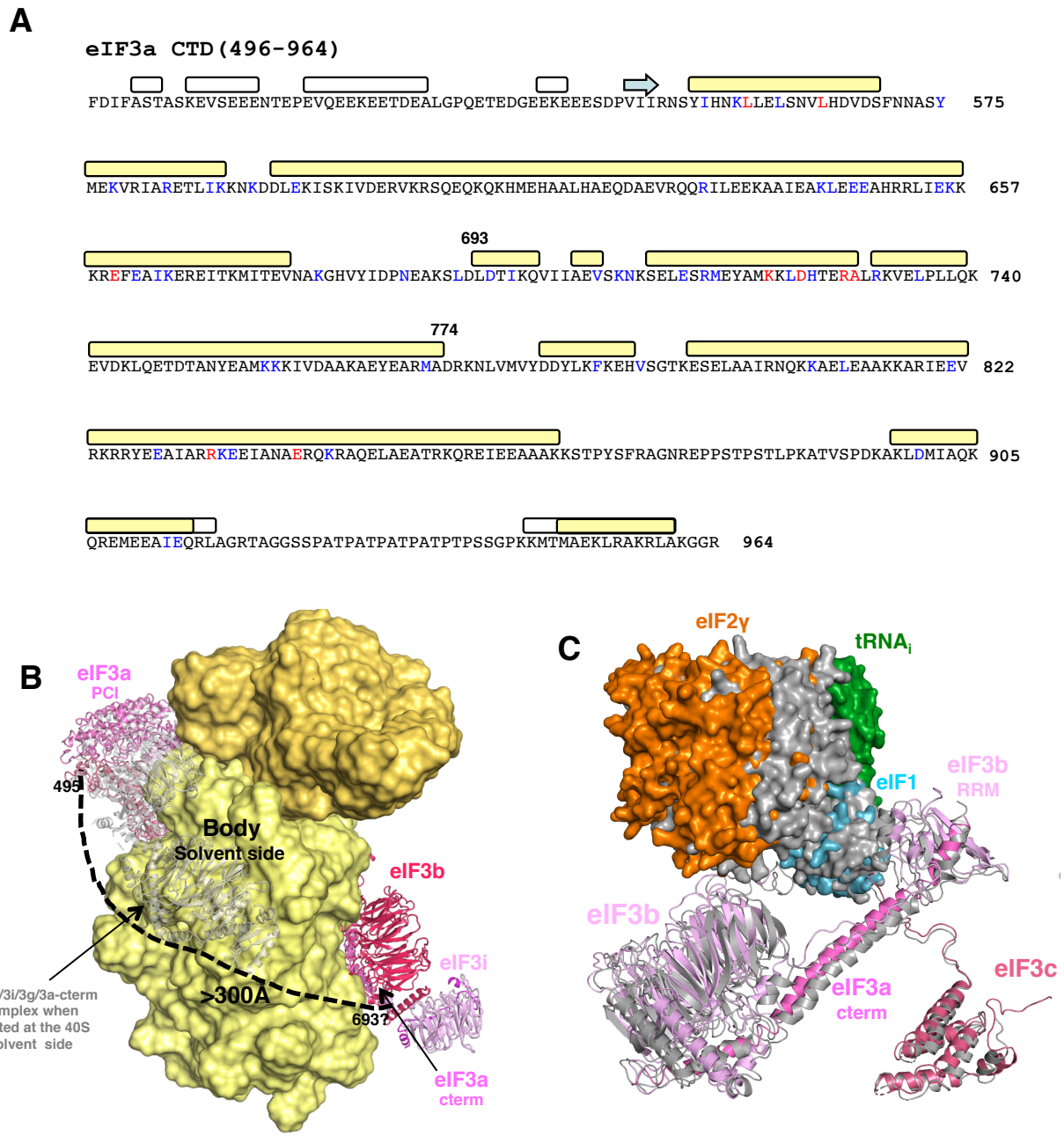
A
eIF3a CTD(496-964)
FDIFASTASKEVSEEENTEPEVQEEKEETDEALGPQETEDGEEKEEESDPVIIRNSYIHNKLLELSNVLHDVDSFNNASY 575
MEKVRIARETLIKKNKDDLEKISKIVDERVKRSQEQKQKHMEHAALHAEQDAEVRQQRILEEKAAIEAKLEEEAHRRLIEKK 657
693
KREFEAIKEREITKMITEVNAKGHVYIDPNEAKSLDLDTIKQVIIAEVSKNKSELESRMEYAMKKLDHTERALRKVELPLLQK 740
774
EVDKLQETDTANYEAMKKKIVDAAKAEYEARMADRKNLVMVYDDYLKFKEHVSGTKESELAAIRNQKKAELEAAKKARIEEV 822
RKRRYEEAIARRKEEIANAERQKRAQELAEATRKQREIEEAAAKKSTPYSFRAGNREPPSTPSTLPKATVSPDKAKLDMIAQK 905
QREMEEAIEQRLAGRTAGGSSPATPATPATPATPTPSSGPKKMTMAEKLRAKRLAKGGR 964
B
eIF3a
PCI
495
Body
Solvent side
eIF3b
eIF3i
>300Å
693?
eIF3b/3i/3g/3a-cterm
complex when
located at the 40S
solvent side
eIF3a
cterm
C
eIF2γ
tRNAi
eIF3b
RRM
eIF1
eIF3b
eIF3a
cterm
eIF3c

Figure 6